www.springer.com/41230
https://doi.org/10.1007/s41230-026-5210-6

Influence of carbon content on precipitated phases and mechanical properties of Nb alloy by vacuum electromagnetic cold crucible melting

Kun Shi[1], Jia-shuo Zhang[1], *Bo-liang Liu[1], Hong-yu Liu[1], Hang Li[2], Jun-xian Wu[2], Shi-bing Liu[1], Wei-chen Qiu[1], Wei-long Wang[1], He-wei Qu[1], and Jia-qi Xie[1]

1. State Key Laboratory of Advanced Casting Technologies, Shenyang Research Institute of Foundry Co., Ltd. CAM, Shenyang 110022, China
2. Unit 93160 of the People's Liberation Army, Beijing 100000, China

Abstract: Nb-5W-2Mo-1Zr-*x*C (*x*=0.04–0.16, wt.%, Nb521 for short) alloys were produced by cold crucible levitation melting (CCLM). The results show that a modest carbon addition (~0.08wt.%) optimizes the strength-ductility balance, whereas further increasing the carbon content yields diminishing strength gains accompanied by a deterioration in ductility. Microstructurally, the low- and medium-carbon alloys are characterized by fine, dispersed NbC and ZrC. In contrast, higher carbon contents promote the formation of irregular, blocky WC precipitates, often accompanied by localized grain-boundary chaining. Mechanical property analysis indicates that strengthening is primarily driven by a combination of solid-solution lattice distortion caused by interstitial carbon and carbide precipitation. The compressive behavior exhibits a strong correlation with the tensile yielding response, serving as an independent validation of the proposed strengthening mechanisms and demonstrating the existence of an optimal carbon range in Nb521 alloys.

Keywords: Nb alloy; carbides; precipitation strengthening; solid-solution strengthening; cold crucible levitation melting

CLC numbers: TG146.4 **Document code:** A **Article ID:** 1672-6421(2026)04-555-11

1 Introduction

Niobium (Nb) and its alloys are distinguished by an exceptional combination of a high melting point (~2,468 °C for Nb) and relatively low density (~8.57 g·cm^{-3}), making them the key candidates among high-temperature structural materials. Notably, among the principal refractory metals (W, Ta, Mo, and Nb), Nb possesses the lowest density while maintaining excellent room-temperature ductility, fabricability, and weldability. These characteristics enable the practical fabrication of complex components[1-3]. In hot-end service environments such as propulsion systems, Nb-based alloys retain useful mechanical properties and formability/weldability at above 1,100 °C and are therefore considered for critical components[4-6].

With rising demands for higher thrust, longer life, and reduced mass, first-generation Nb alloys (e.g., Nb-10Hf-1Ti, C-103) are nearing their temperature limits; even with oxidation-resistant coatings, their stable operating temperature is typically ~1,400 °C[7, 8]. To further extend the temperature window and specific strength, multicomponent Nb-W-based alloys have emerged for hot-section applications. A representative grade, Nb521, relies on its high solid-solution strengthening from W and Mo together with Zr-induced carbide-precipitation strengthening, delivers markedly superior high-temperature strength and creep resistance compared with the first-generation Nb alloys; in conjunction with compatible silicide-type oxidation-resistant coatings, the coated maximum service temperature can reach ~1,600 °C[9]. Recent comparisons between C-103 and Nb521 at 1,300 °C also show that Nb521 attains a higher yield strength and a significantly lower steady-state creep rate, indicating better high-temperature load-bearing capability and microstructural stability[1].

***Bo-liang Liu**

Male, doctoral candidate. His research primarily focuses on refractory alloys, levitation melting, additive manufacturing, and the relationship between microstructure and mechanical properties of high performance metallic materials.

E-mail: liubl435871@126.com

Received: 2025-09-01; Revised: 2025-11-03; Accepted: 2025-11-18

Nevertheless, producing multicomponent refractory alloys in large sizes with high purity and good homogeneity remains a key bottleneck. Conventional vacuum arc/induction melting, when applied to chemically active systems with large disparities in melting point and density, is prone to crucible reactions and contamination, elemental losses, and segregation; achieving uniform composition and microstructure often requires multiple remelts, increasing both cost and contamination risk[10]. To mitigate these root causes at the process level, cold crucible levitation melting (CCLM) has attracted considerable attention. CCLM employs a water-cooled segmented copper crucible and a high-frequency induction field to levitate the molten metal and impose strong electromagnetic stirring, thereby avoiding direct melt-crucible contact and enabling rapid attainment of a high-temperature, high-purity, and highly homogeneous melt[10–12]. For systems with pronounced melting-point/density contrasts that are difficult to homogenize in a single melt (e.g., Ti-Ta), CCLM has demonstrably produced ~1 kg homogeneous ingots in one pass[13], underscoring its suitability for reactive, segregation-prone refractory multicomponent alloys. For Nb-W-Mo-Zr systems, adopting CCLM reduces crucible-induced contamination and segregation while improving homogeneity and scale-up feasibility[10–12].

Microalloying is an effective route to enhance the high-temperature load-bearing capacity and stability of Nb-based alloys. Interstitial carbon can form stable carbides with refractory elements such as Zr, Nb, and W (e.g., ZrC, Nb_2C), providing dispersion strengthening and grain-boundary pinning that improve strength, creep resistance, and microstructural stability. This strategy has been validated in the Mo-based TZM alloy (Mo-0.5Ti-0.1Zr-0.02C)[14]. In Nb-based systems, long-term creep studies on PWC-11 (Nb-1Zr-0.1C) show that fine, stable (Zr,Nb)C precipitates markedly increase the rupture strength near 1,350 K (by multiples compared with carbon-free Nb alloy)[15]. Recent work on Nb-W-Mo-Zr alloys observes the formation of (Nb,Zr)C and Nb_2C under suitable thermal histories, benefiting high-temperature strength and stability[16]. It must be emphasized that the carbon content should be tightly controlled within a narrow window: excessive, continuous-network, or coarsened carbides can induce brittleness and second-phase segregation, degrading toughness and weldability[14–16]. Consequently, selecting a melting route that enables rapid homogeneous melting with minimal contamination, such as CCLM, is critical to ensure sufficient carbon dissolution and dispersed distribution[17, 18].

On this basis, this study employed CCLM to synthesize Nb521 (Nb-5W-2Mo-1Zr) with varying carbon levels, aiming to obtain high-purity, highly homogeneous feedstock under crucible-free conditions under strong electromagnetic force. Subsequent microstructural characterization and mechanical testing were used to elucidate how trace carbon modulates microstructural evolution, the formation and distribution of carbide second phases, and macro- and micro-scale compositional homogeneity in Nb521, thereby clarifying the strengthening mechanisms and providing a foundation for the design and manufacture of Nb-W refractory alloys targeted at higher temperature regimes and more complex components.

2 Experimental procedure

2.1 Raw materials preparation

High-purity Nb, W, Mo, and Zr metals together with graphite were used as raw materials. The raw charge was weighed to achieve a target composition of Nb-5wt.%W-2wt.%Mo-1wt.%Zr-*x*wt.%C (where x = 0.04, 0.08, 0.12, and 0.16), with a total mass of 5 kg. Prior to weighing, all metallic feedstock was mechanically polished to remove surface oxides, ultrasonically cleaned in anhydrous ethanol for 15 min, and then, dried, and stored in a clean, dry environment to minimize adsorbed moisture and extraneous contamination.

2.2 Cold crucible levitation melting (CCLM)

Alloys were prepared using an in-house medium-frequency induction CCLM apparatus, comprising a water-cooled segmented copper crucible, an induction-coil system, and a high-vacuum chamber. Pre-treated feedstock was placed at the crucible center, the chamber was evacuated to ~10^{-2} Pa, and then backfilled with high-purity Ar (99.999%) to 0.02 MPa to establish a protective atmosphere. An alternating magnetic field was generated by applying electrical power, inducing eddy-current heating and achieving non-contact levitation heating with strong electromagnetic stirring. The melt was held for approximately 10 min to enhance compositional homogeneity, after which the power was shut off and the furnace cooled synchronously; solidification of Nb521 ingots was proceeded under an Ar backfill pressure.

2.3 Microstructural characterization

Samples were ground and polished following standard metallographic practice and then etched using 30 mL HNO_3+10 mL HF+60 mL H_2O to reveal grain boundaries. Optical microscopy (OM) provided initial microstructural observations. Scanning electron microscopy (SEM) equipped with energy-dispersive X-ray spectroscopy (EDS) was employed to analyze the morphology and composition of nanoscale precipitates. Phase identification was analyzed using X-ray diffraction (XRD) with a scan range of 20°–100° at 4°·min^{-1}. TEM/STEM foils were prepared by FIB lift-out technique to fabricate a single-lamella and were subsequently examined at 200 kV in both HRTEM and selected-area electron diffraction (SAED) modes. For acicular and banded/blocky second phases, SAED spots, zone axes, and interplanar spacings (d) were recorded. FFTs of HRTEM lattice images were used to index the {hkl} and OA/OB directions, and to check their consistency with PDF data.

2.4 Mechanical testing

As shown in Fig. 1, the tensile specimens measured a geometry of M6×Φ3 mm and were tested at room temperature

at a constant withdrawal rate speed of 1 mm·min^{-1}. Following the Chinese National Standard GB/T228.1-2021, the 0.2% offset yield strength ($R_{p0.2}/\sigma_{0.2}$), ultimate tensile strength (UTS), elongation to failure (A), and reduction of area (Z) were determined. Compression tests were conducted on cylindrical specimens with dimensions of Φ10 mm×20 mm, featuring ground, parallel end faces. The tests were performed at room temperature in accordance with the Chinese National Standard GB/T 7314-2017, using lubrication or low-friction platens to reduce end effects. The measured mechanical response yielded the compressive 0.2% yield strength, true stress-strain curves, and the elastic modulus.

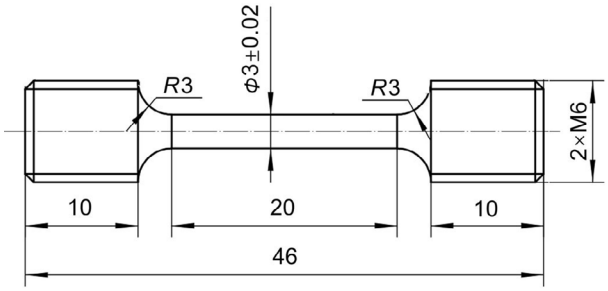

Fig. 1: Schematic of tensile specimen (Unit: mm)

3 Results

3.1 Thermodynamic calculations of carbides

Carbides exist in alloys due to the following reactions:

$$\mathrm{Zr(s)+C(s)\rightarrow ZrC(s)} \quad (1)$$

$$\mathrm{Nb(s)+C(s)\rightarrow NbC(s)}v_i \quad (2)$$

$$\mathrm{W(s)+C(s)\rightarrow WC(s)} \quad (3)$$

To determine the direction of reactions, the Gibbs free energy (ΔG) and the enthalpy change (ΔH) were computed using the Gibbs-Helmholtz equation[19-20]:

$$\Delta H^{\circ}_{298}=\Sigma_i \Delta H^{\circ}_{f,i}(298) \quad (4)$$

$$\Delta S^{\circ}_{298}=\Sigma_i v_i S^{\circ}_i(298) \quad (5)$$

where v_i denotes the stoichiometric coefficient (positive for products and negative for reactants); ΔH°_{298} and ΔS°_{298} are the standard enthalpy and entropy changes of the reaction at 298 K, respectively; $\Delta H^{\circ}_{f,i}(298)$ is the standard enthalpy of formation of species (i) at 298 K (kJ·mol^{-1}), and $S^{\circ}_i(298)$ is the standard entropy of species (i) at 298 K (J·mol^{-1}·K^{-1}). All values were calculated based on per mole of carbon.

The molar heat capacity of species i at temperature T is expressed as:

$$C_{p,i}(T)=a_i+b_iT+c_iT^{-2}+d_iT^2 \quad (6)$$

where a_i, b_i, c_i, d_i are the heat capacity fitting coefficients for species (i), which correspond to the constant, linear, inverse-square, and quadratic temperature terms, respectively, and are valid over a specified temperature range.

The net heat capacity for the reaction is given by:

$$\Delta C_p(T)=\sum_i v_i C_{p,i}(T) \quad (7)$$

The standard enthalpy changes at temperature T is obtained by integrating the heat capacity:

$$\Delta H^{\circ}(T)=\Delta H^{\circ}_{298}+\int_{298}^{T}\Delta C_p(T)\mathrm{d}T \quad (8)$$

Similarly, the standard entropy change is:

$$\Delta S^{\circ}(T)=\Delta S^{\circ}_{298}+\int_{298}^{T}\frac{\Delta C_p(T)}{T}\mathrm{d}T \quad (9)$$

For clarity, the closed-form expressions for these integrals, derived using polynomial expressions for C_p are:

$$\Delta H^{\circ}(T)=\Delta H^{\circ}_{298}+A(T-298)+\frac{B}{2}(T^2-298^2)+\frac{C}{3}(T^3-298^3)-D\left(\frac{1}{T}-\frac{1}{298}\right) \quad (10)$$

$$\Delta S^{\circ}(T)=\Delta S^{\circ}_{298}+A\ln\frac{T}{298}+B(T-298)+\frac{C}{2}(T^2-298^2)-\frac{D}{2}\left(\frac{1}{T^2}-\frac{1}{298^2}\right) \quad (11)$$

In these equations, A, B, C, and D are the coefficients derived from the heat capacity of the Reactions (1)–(3), as given by the expression for ΔC_p in Eq. (6).

$$\Delta G^{\circ}(T)=\Delta H^{\circ}(T)-T\Delta S^{\circ}(T) \quad (12)$$

Based on Eq. (10), the standard Gibbs free energy of formation for each reaction can be expressed as a temperature dependent linear relation:

$$\Delta G^{\circ}_f(T)=A_i+B_iT \quad (13)$$

where A_i and B_i are the coefficients for each reaction[21, 22]. The standard Gibbs free energy of formation is then obtained after unit conversion:

$$\Delta G^{\circ}_f=\frac{(A_i+B_iT)\times 4.184}{1000} \quad (14)$$

Based on the above thermodynamic calculations, Fig. 2 presents the temperature dependent [$\Delta H^{\circ}(T)$] and [$\Delta G^{\circ}(T)$] curves for the formation of ZrC, NbC, and WC over the temperature range of 1,000–3,000 K. Figure 2(a) demonstrates that Zr+C→ZrC is the most exothermic reaction across this temperature range, with a reaction enthalpy 50–60 kJ·mol^{-1} more negative than that of Nb+C→NbC, which in turn is more exothermic than W+C→WC. Figure 2(b) shows the Gibbs free energy change [$\Delta G^{\circ}(T)$] for the three reactions (1) to (3). All the curves become less negative with increasing temperature, reflecting the increasing dominance of this term at higher temperatures. Nevertheless, Reaction (1) maintains the most negative throughout the 1,000–3,000 K range, indicating that Zr+C→ZrC is the most thermodynamically favourable of the three reactions. Thus, at any given temperature within the 1,000–3,000 K range, Reaction (1) is predicted to release the most free energy, followed by Reaction (2), and Reaction (3) is the least favorable.

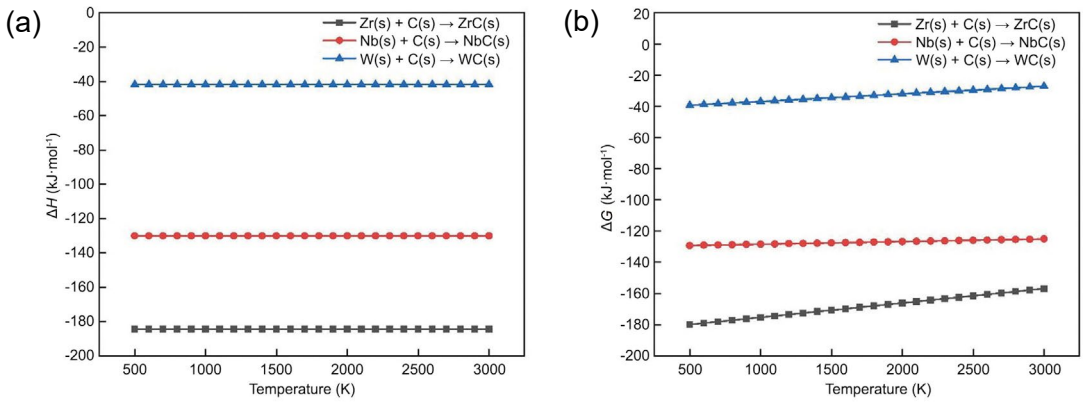

Fig. 2: Temperature dependent curves of Δ*H* (a) and Δ*G* (b) for carbon reactions in Nb521

3.2 Microstructure and secondary phases

Figure 3 shows the microstructure of Nb521 with different carbon contents. The matrix exhibits a single-phase equiaxed grain morphology, while the morphology and distribution of precipitates vary markedly with carbon content. Figures 3(a–d) present the microstructures of Nb521 with 0.04wt.% and 0.08wt.% C, in which only acicular precipitates are observed uniformly and finely dispersed along grain boundaries and within grains. Figures 3(e–h) display the microstructures at higher carbon contents (0.12wt.% and 0.16wt.% C): the

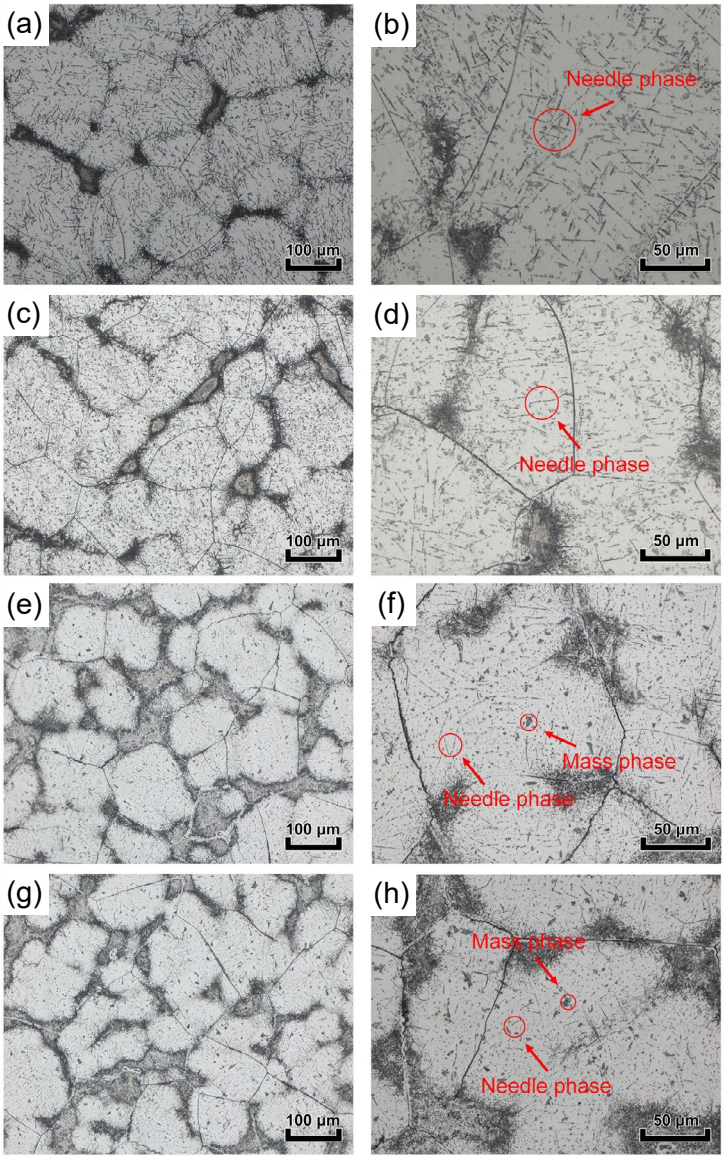

Fig. 3: Microstructure morphology of Nb521 alloy with different C contents: (a), (b) 0.04wt.%; (c), (d) 0.08wt.%; (e), (f) 0.12wt.%; (g), (h) 0.16wt.%

size and distribution of the acicular phase remain essentially unchanged, but blocky precipitates appear intragranularly at 0.12wt.% C and increase in number density with further carbon addition up to 0.16wt.% C.

To analyze the composition of the blocky precipitates, SEM was performed. As shown in Fig. 4, these precipitates are irregularly blocky and generally smaller than 10 μm, with polygonal outlines and sharp interfaces in the EDS images. The corresponding EDS area maps (Fig. 5) show pronounced enrichment of W and C within the precipitates, while Nb and Zr signals are markedly attenuated and remain uniform only in the matrix, indicating that the blocky phase is typical WC carbide.

Figure 6 shows the microstructure analysis of the needle like phase. Figures 6(a–c) show representative TEM characterizations of NbC-type carbides. In the high-resolution TEM image [Fig. 6(b)], well-ordered lattice fringes with a measured spacing of ~2.27 Å are observed, which correspond to the {111} planes of fcc-NbC. The SAED pattern in Fig. 6(c), acquired along the [0-1-1] zone axis, exhibits sharp diffraction spots. The indexed reflections, including (-11-1), (11-1), and (200), are consistent with the fcc-NbC structure (space group Fm-3m), confirming the presence of the NbC phase. Elemental maps in Figs. 6(d–h) indicate that this phase primarily consists of Nb and C, with no obvious enrichment of Mo or Zr, again supporting its identification as NbC. Morphologically, the NbC particles exhibit an acicular (needle-like) or fine-rod morphology, are homogeneously dispersed within the matrix grains, and effectively pin dislocations, thereby imparting significant precipitation strengthening.

The TEM results in Figs. 7(a–c) correspond to ZrC-type carbides. Bright-field images reveal an acicular morphology; in the HRTEM image [Fig. 7(b)], lattice fringes with spacings of ~2.62 Å and ~2.50 Å can be assigned to the {111} and {200} planes of fcc-ZrC, respectively. The SAED pattern [Fig. 6(c)] further validates this assignment with a [0-1-1] zone axis, fully consistent with PDF data for ZrC. The indexed spots

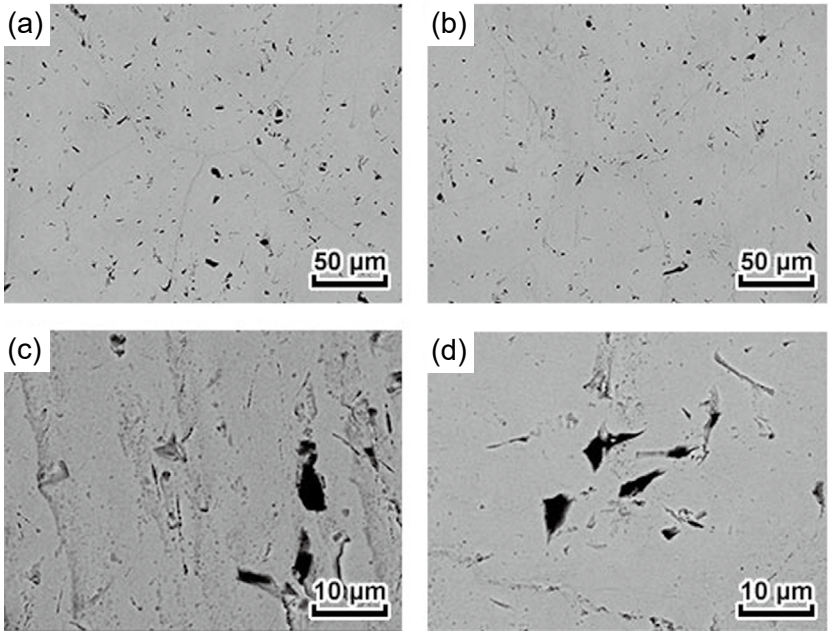

Fig. 4: Block-like phase morphology (a–d)

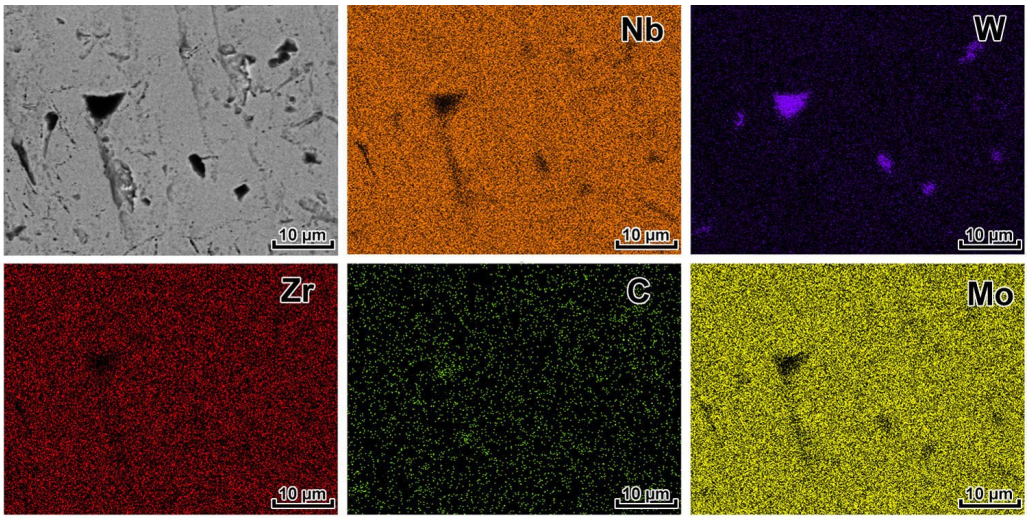

Fig. 5: Distribution of block phase elements

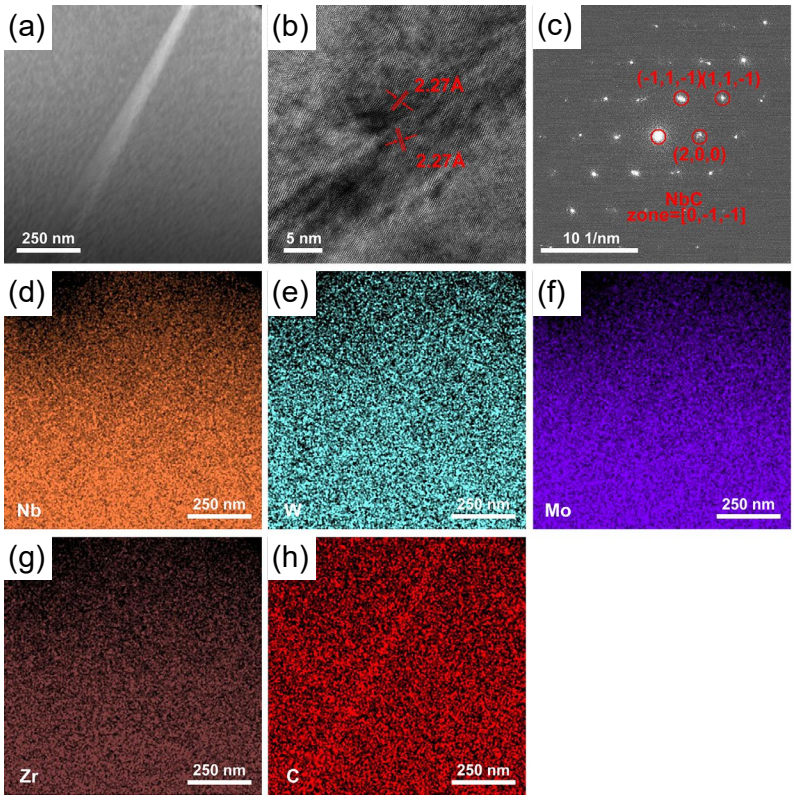

Fig. 6: Needle-like phase morphology and element distribution of NbC-type carbides: (a) phase morphology; (b) TEM high-resolution image; (c) phase diffraction points; (d–h) phase element distribution

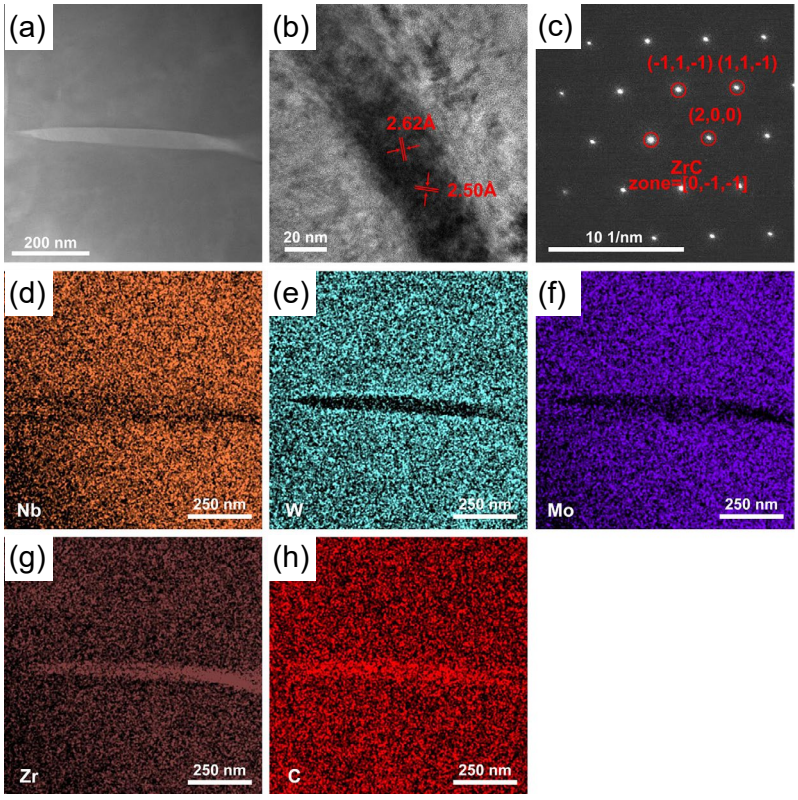

Fig. 7: ZrC-type carbide morphology and element distribution of ZrC-type carbides: (a) phase morphology; (b) TEM high-resolution image; (c) phase diffraction points; (d–h) phase element distribution

correspond to {111} and {200} reflections. EDS maps in Figs. 6(d–h) show pronounced enrichment of C and Zr within the needle-like or bonded features, with only minor Nb in solid solution and no discernible enrichment of W or Mo. This compositional signature supports their identification as ZrC-type carbides. These ZrC precipitates are predominantly located at along grain boundaries, with a fraction is also dispersed inside grains.

XRD analyses in Fig. 8(a) further elucidate phase constitution versus carbon content. All compositions exhibit the characteristic bcc-Nb matrix reflections corresponding to the (110), (200), (211), and (220) planes. As shown in Fig. 8(b), increasing C from 0.04wt.% to 0.16wt.% causes a systematic shift of the matrix (110) peak to higher angles by ~0.2°, indicating a slight contraction of the lattice parameter.

According to Bragg's law[1]:

$$2d\sin\theta = n\lambda \quad (14)$$

where d is the interplanar spacing, θ is the Bragg angle, λ is the X-ray wavelength, and n is the diffraction order. The observed peak shift is attributable to a combination of changes in solid-solution chemistry and lattice microstrain. As the carbon content increases, interstitial dissolution of C in the Nb matrix and precipitation of larger atoms from the matrix subtly modify the matrix composition and induce solid-solution distortion, which in turn contracts the lattice slightly and shifts the matrix peaks to higher 2θ angles.

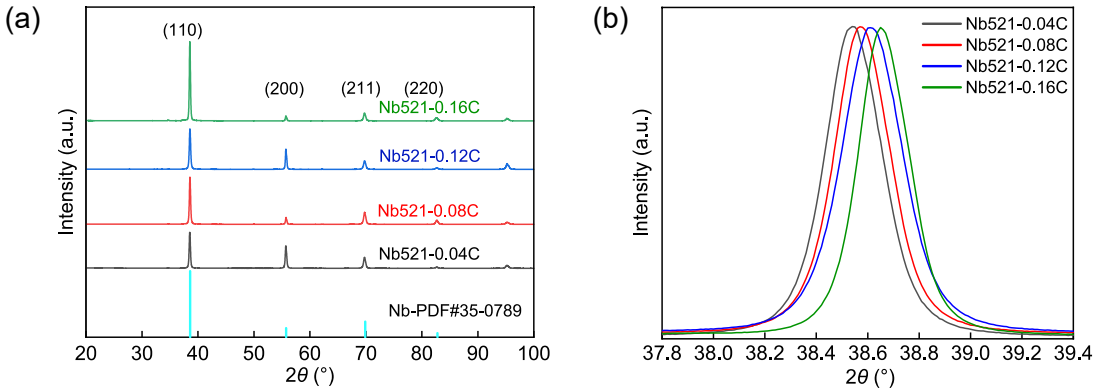

Fig. 8: XRD diffraction patterns of Nb521 alloys with different C contents (a) and (110) peak offset (b)

3.3 Mechanical properties

Tables 1 and 2 summarize the room-temperature tensile and compressive properties of Nb521 with different carbon contents; the corresponding stress-strain curves are shown in Figs. 9(a, b). Increasing C from 0.04wt.% to 0.08wt.% enhances strength and ductility concurrently: at 0.08wt.% C, yield strength (YS) and UTS reach 382±7 MPa and 547±7 MPa, respectively, compared with 368±7 MPa and 510±6 MPa at 0.04wt.% C, while elongation increases from (9.5±1)% to (13±0.2)%, achieving a more favorable strength-ductility balance. Further increasing C to 0.12wt.% and 0.16wt.% degrades tensile performance: YS falls to 355±5 MPa and 319±9 MPa, UTS decreases to 466±12 MPa and 347±7 MPa, and elongation drops to (3.5±1)% and (2.5±0.2)%, indicating pronounced embrittlement at high carbon levels. The compression stress-strain curves are shown in Figs. 9(c, d). Compression results mirror these trends and provide strong cross-validation. The 0.04wt.% C alloy exhibits a compressive yield strength (CYS, determined by the 0.2% offset method) of 380±23 MPa and high compressive plasticity of (75±4)%. With increasing carbon content to 0.08wt.%, the CYS increases to 405±2 MPa, while the compressive plasticity remains high at (74±0.5)%, indicating the best overall balance between strength and plasticity among the investigated alloys. At 0.12wt.% and 0.16wt.% C, CYS decreases to 364±6 MPa and 348±9 MPa, respectively, and compressive plasticity declines to (59.5±1)% and (59±0.5)%. These trends are consistent with the tensile observations, which indicate strength saturation or decline accompanied by a significant loss of ductility. Consequently, a carbon content of 0.08wt.% yields the best synergy of strength and plasticity in Nb521 at room temperature, whereas exceeding this window leads to concomitant deterioration in both properties.

Table 1: Mechanical properties of Nb521 alloys with different carbon contents

Carbon content	YS (MPa)	UTS (MPa)	Elongation (%)
0.04wt.%	368±7	510±6	9.5±1
0.08wt.%	382±7	547±7	13±0.2
0.12wt.%	355±5	466±12	3.5±1
0.16wt.%	319±9	347±7	2.5±0.2

Table 2: Compressive properties of Nb521 alloys with different carbon contents

Carbon content	CYS (MPa)	Elongation (%)
0.04wt.%	380±23	75±4
0.08wt.%	405±2	74±0.5
0.12wt.%	364±26	59.5±1
0.16wt.%	348±9	59±0.5

Figure 10 shows that the tensile fracture surfaces reveal composition-dependent fracture modes. At 0.04% and 0.08% C, the fractures are dominated by cleavage or quasi-cleavage, characterized by broad, flat cleavage facets/steps and straight tear ridges, with no discernible dimples. At 0.12wt.% and 0.16wt.% C, brittle transgranular fracture prevails. The increased population of carbides markedly reduces fracture resistance by limiting plastic energy absorption prior to failure.

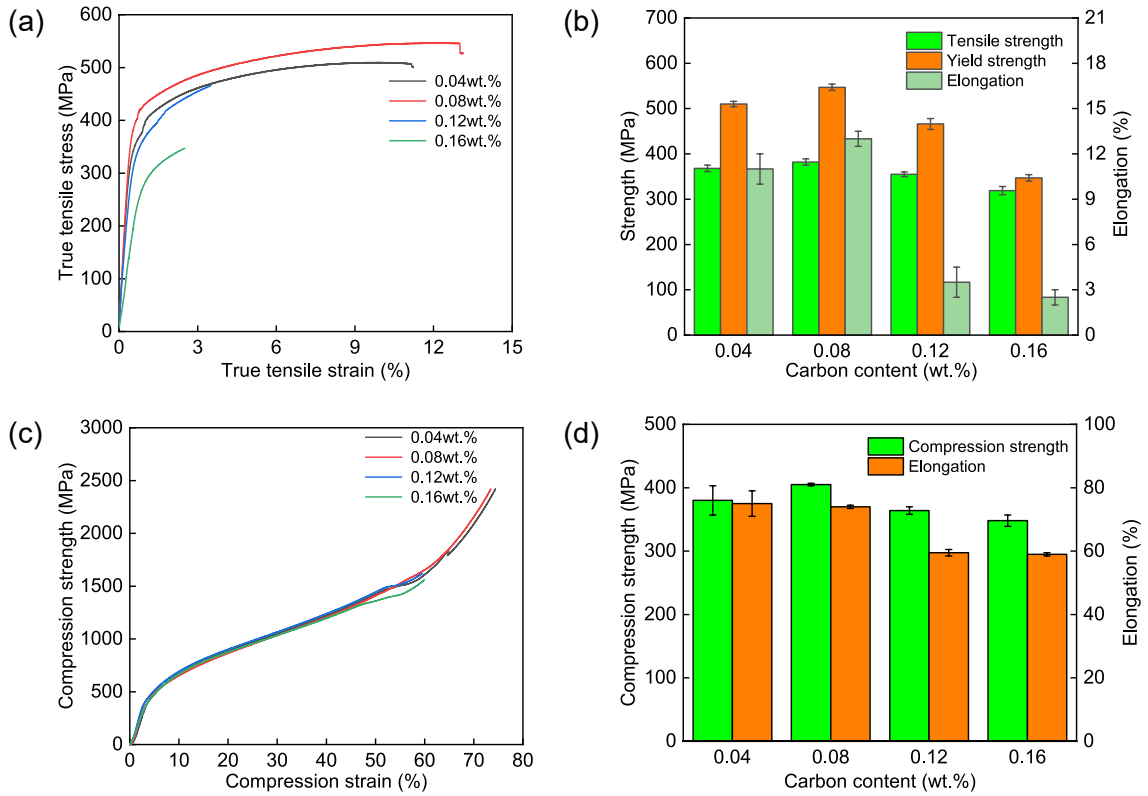

Fig. 9: Mechanical properties of Nb521 alloys with different carbon contents: (a), (b) tensile properties; (c), (d) compressive properties

4 Discussion

As the carbon content increases from 0.04wt.% to 0.08wt.% in Nb-5W-2Mo-1Zr (Nb521), the yield strength rises markedly, attributable to the cooperative action of multiple carbon-induced strengthening mechanisms interstitial solid-solution distortion and carbide precipitation acting in concert[21-23]. The yield strength can be written as the sum of individual contributions, as follows:

$$\sigma_y = \sigma_0 + \Delta\sigma_{ss} + \Delta\sigma_p + kd^{-1/2} \quad (15)$$

where σ_0 is the intrinsic matrix strength, $\Delta\sigma_{ss}$ is the solid-solution strengthening increment, $\Delta\sigma_p$ is the precipitation strengthening increment, and the term $kd^{-1/2}$ represents the Hall-Petch grain-refinement contribution. Carbon raises the strength mainly via solid-solution and precipitation mechanisms; as evidenced by Fig. 3, the grain size remains essentially unchanged across the carbon levels, indicating that the Hall-Petch contribution can be neglected. Accordingly, the following focuses on how carbon content affects $\Delta\sigma_{ss}$ and $\Delta\sigma_p$.

4.1 Solid solution strengthening

As the carbon content in the Nb521 alloy increases, carbon dissolves interstitially in the Nb matrix and markedly impedes dislocation motion, thereby enhancing the yield strength. This arises from the atomic size and elastic-modulus mismatch between solute and matrix atoms, which generates lattice distortions and local stress fields that impede dislocation glide. Because the atomic radius of C is much smaller than that of Nb, interstitial C produces substantial lattice strain; it may also perturb the local elastic modulus. Collectively, these effects elevate the stress required for dislocations to shear or bypass solute fields and thus strengthen the alloy.

The increment in yield stress can be quantified using the solid-solution strengthening model, as shown in Eq. (16):

$$\Delta\sigma_{ss} = \frac{A}{b}\left(\frac{F_m^4\varepsilon_L}{\Gamma}\right)^{1/3}\left(\frac{c}{l^2}\right)^{2/3} \quad (16)$$

where $A\approx1$; b is the Burgers vector of Nb (b=0.2858); F_m is the maximum solute-dislocation interaction force; ε is the interaction range with $\varepsilon=2d$, and d is the Nb lattice spacing (d=0.233). The dislocation line tension is $\Gamma \approx \mu b^2/2 \approx 3.03\times10^6$ (with μ=37.5 GPa, is the shear modulus of Nb). The solute concentration increment is taken as c=0.003at.%, and the characteristic length l is evaluated from the dislocation line-spacing expression.

The maximum solute-dislocation interaction force F_m is given by Eq. (17):

$$F_m = \frac{\mu b^2}{\phi} \quad (17)$$

where ϕ is a dimensionless geometrical factor for the solute-dislocation elastic interaction, taken as 6 in this calculation. ε_L is the combined misfit strain incorporating shear-modulus and lattice-parameter misfits, as follows:

$$\varepsilon_L = \left[\left(\frac{\varepsilon_\mu}{1+0.5|\varepsilon_\mu|}\right)^2 + (\alpha\varepsilon_b)^2\right]^{2/3} \quad (18)$$

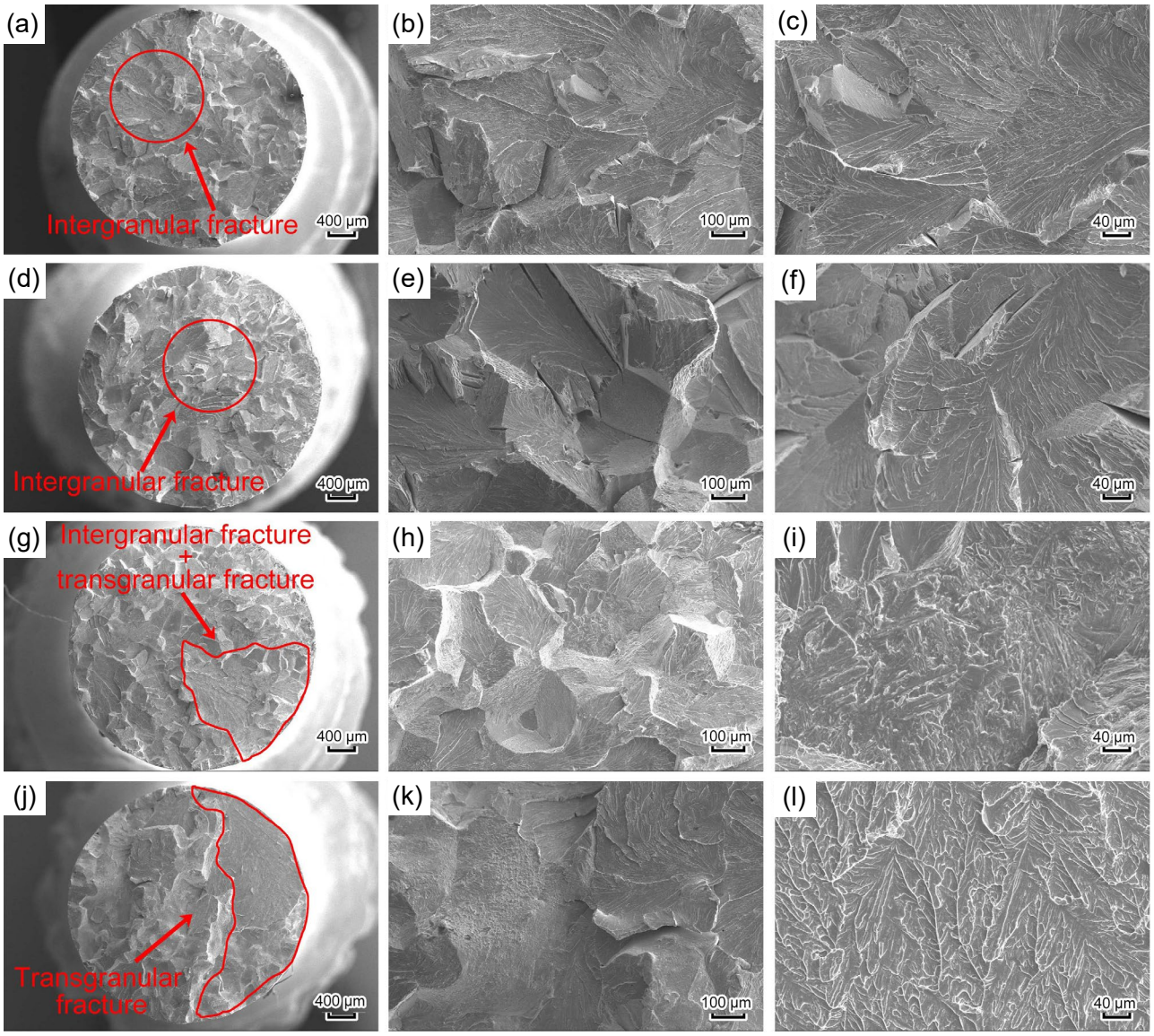

Fig. 10: Tensile fracture surfaces of Nb521 alloys with different C contents: (a–c) 0.04wt.%; (d–f) 0.08wt.%; (g–i) 0.12wt.%; (j–l) 0.16wt.%

where ε_μ is the shear-modulus misfit parameter between interstitial C atoms and the Nb matrix, ε_b is the lattice-parameter or atomic-size misfit parameter, and α is a dimensionless weighting coefficient for the size-misfit contribution. In this calculation, ε_μ=0.10, ε_b=0.233, and α=16.

The dislocation line spacing for C in Nb is estimated as Eq. (19):

$$l = \left(\frac{2}{c^{1/3}} - 3\right) b + (b + b_{sol}) \tag{19}$$

where b_{sol} is the effective atomic diameter, or characteristic atomic spacing, of the solute atom used in estimating the mean dislocation line spacing; in this calculation, b_{sol}=0.3647 nm.

Based on this model, as the carbon content increases, interstitial-carbon-induced lattice distortion and local stress fields lead to a discernible rise in yield strength. For an increment of 0.04wt.% C, the solid-solution increment is about 14 MPa, indicating that carbon in solid solution makes a measurable contribution to strengthening through its interaction with dislocations.

4.2 Precipitation strengthening

As the carbon content increases, the strengthening of Nb521 is driven not only by solid solution strengthening but also by the formation of finely dispersed carbide precipitates, which provide significant precipitation hardening[21]. The addition of 1wt.% Zr together with trace C is intended to generate stable carbides in the matrix (e.g., ZrC and Nb_2C) that impede dislocation motion and enhance high-temperature strength. With increasing carbon content, the number density of precipitates increases and the mean inter-particle spacing decreases. Consequently, higher stresses are required for dislocations to bypass the particles via the Orowan mechanism. According to this mechanism, the contribution of precipitation to the yield strength can be calculated as Eq. (19):

$$\Delta\sigma_p = M \cdot 0.045 \frac{\mu_b}{\lambda} \ln\left(\frac{r}{b}\right) \tag{20}$$

where M is the polycrystalline Taylor factor (for Nb, M≈3), λ is the mean inter-particle spacing (λ=400 nm), and r is the average precipitate radius (r≈5 μm).

The calculated precipitation strengthening increment is about 20 MPa. At higher carbon contents, finely dispersed acicular precipitates form in Nb521, which effectively pin dislocations and markedly increase the yield strength. Through the Orowan bypass mechanism, their strengthening contribution increases as the precipitate number density rises and the spatial distribution becomes more favorable.

From the foregoing mechanistic analysis and quantitative checks, it can be concluded that an intermediate carbon level in Nb521 (≈0.08wt.% C) is optimal for strengthening. At this composition, solid-solution and precipitation mechanisms act cooperatively, maximizing both the matrix resistance to dislocation glide and the carbide pinning. Meanwhile, the carbides maintain a favorable morphology, fine and well dispersed, without introducing pronounced brittle microstructural features. As a result, the alloy attains a high yield strength (and hardness) while retaining a good ductility. In contrast, at higher carbon contents (e.g., 0.16 wt.%), excessive precipitation leads to detrimental microstructural features, including carbide coarsening and grain-boundary chaining. These changes increase the effective inter-particle spacing (λ), thereby reducing strengthening efficiency. Concurrently, the large carbides disrupt matrix load continuity and decrease the work-hardening rate (θ), promoting strain localization and ultimately causing a decline in both strength and toughness. Experimentally, this manifests as a plateau in yield-strength at 0.16wt.% C, accompanied by slight decreases in UTS and elongation.

5 Conclusions

This study investigates the interplay between carbon content, microstructure, properties, and strengthening mechanisms in Nb-5W-2Mo-1Zr-xC alloys prepared by cold crucible levitation melting (CCLM). By employing multiscale microstructural characterization (OM/SEM/TEM-EDS, XRD) and room-temperature mechanical testing, a mechanistic framework for composition optimization is established. Following conclusions are obtained:

(1) The carbides in the Nb521 alloy, primarily NbC and ZrC, are uniformly dispersed within the grains and along the grain boundaries. Thermodynamic calculations predict that NbC and ZrC precipitate first, leading to a stable microstructure. However, as the carbon content increases to no less than 0.12wt.% C, the formation of irregular, blocky WC precipitates becomes more pronounced. The excess carbon favors the precipitation of WC, which is accompanied by increased inter-particle spacing, thereby compromising the stability.

(2) At 0.08wt.% C, Nb521 alloys exhibit the optimal balance of strength and ductility, with yield strength increasing from 368±7 MPa at 0.04wt.% C to 382±7 MPa, and ultimate tensile strength (UTS) rising from 510±6 MPa to 547±7 MPa. Elongation also improves, increasing from (9.5±1)% to (13±0.2)%, achieving a more favourable strength-ductility balance. However, at 0.12wt.% and 0.16wt.% C, all mechanical properties, YS, UTS, and elongation, decline, indicating pronounced embrittlement. The strengthening mechanism is primarily due to interstitial-carbon solid-solution lattice distortion and Orowan bypass by fine carbides. At higher carbon levels, carbide coarsening and grain-boundary segregation lead to a loss in ductility and a decrease in the overall strengthening efficiency.

Acknowledgment

The work was supported by the Liaoning Province Science and Technology Plan Project (Project No. 2023JH2/101700049).

Conflict of interest

The authors declare that they have no conflict of interest to declare.

References

[1] Brizes E, Milner J A. A comparison of niobium alloys C103 and Nb521. In: Proceedings of the TMS 2025 Annual Meeting & Exhibition. The Minerals, Metals & Materials Society, 2025, Available via NASA Technical Reports Server.
[2] ASM International. Refractory metals and alloys. In: Davis J R (Ed.), Metals Handbook Desk Edition, 2nd ed., ASM International, Materials Park, OH, 1998.
[3] Royal Society of Chemistry. Niobium–Element information, periodic table. https://periodic-table.rsc.org/element/41/niobium, accessed September 1, 2025.
[4] He X, Zhang X, Li Y, Huang J, et al. Effect of Mo on microstructure and mechanical properties of Nb-Ti-C-B multiphase alloy. Journal of Alloys and Compounds, 2013, 551: 578–583. https://doi.org/10.1016/j.jallcom.2012.11.052.
[5] Kim W Y, Tanaka H, Kasama A, et al. Effect of carbon on the tensile properties of Nb-Mo-W alloys at 1,773 K. Journal of Alloys and Compounds, 2002, 333(1–2): 170–178.
[6] Sankar M, Satya P V V, Baligidad R G, et al. Effect of vacuum arc remelting and processing parameters on structure and properties of high purity niobium. International Journal of Refractory Metals and Hard Materials, 2015, 50: 120–125. https://doi.org/10.1016/j.ijrmhm.2014.12.001.
[7] Sankar M, Baligidad R G, Gokhale A A. Effect of oxygen on microstructure and mechanical properties of niobium. Materials Science and Engineering: A, 2013, 569: 132–136. https://doi.org/10.1016/j.msea.2013.01.025.
[8] Aggarwal G, Park S J, Smid I. Development of niobium powder injection molding: Part I. Feedstock and injection molding. International Journal of Refractory Metals and Hard Materials, 2006, 24(3): 253–262. https://doi.org/10.1016/j.ijrmhm.2005.06.003.
[9] Aggarwal G, Smid I, Park S J, et al. Development of niobium powder injection molding. Part I: Debinding and sintering. International Journal of Refractory Metals and Hard Materials, 2007, 25(3): 226–236. https://doi.org/10.1016/j.ijrmhm.2006.05.005.
[10] Pericleous K, Bojarevics V, Djambazov G, et al. Experimental and numerical study of the cold crucible melting process. Applied Mathematical Modelling, 2006, 30(11): 1262–1280. https://doi.org/10.1016/j.apm.2006.03.003.
[11] Gagnoud A, Etay J, Garnier M. The levitation melting process using cold crucible technique. ISIJ International, 1988, 28: 36–40. https://doi.org/10.2355/isijinternational1966.28.36.

[12] Morita A, Fukui H, Tadano H, et al. Alloying titanium and tantalum by cold crucible levitation melting furnace. Materials Science and Engineering: A, 2000, 280(1): 208–213. https://doi.org/10.1016/S0921-5093(99)00668-1.
[13] Fukui H, Yang W, Okae F, et al. Cold crucible levitation melting of biomedical Ti-30wt.%Ta alloy. Dental Materials Journal, 2001, 20(2): 156–163. https://doi.org/10.4012/dmj.20.156.
[14] Metzger F, Rienzi V, Mascetti C, et al. Properties of titanium zirconium molybdenum alloy after exposure to indium at elevated temperatures. Materials, 2022, 15(15): 5270. https://doi.org/10.3390/ma15155270.
[15] Titran R H, Moore T J, Grobstein T L. Creep behavior of niobium alloy PWC-11, NASA Technical Memorandum 89834. National Aeronautics and Space Administration, Lewis Research Center, Cleveland, OH, 1987. https://ntrs.nasa.gov/citations/19870010972, accessed September 1, 2025.
[16] Yang J, Huang Y, Liu B, et al. Precipitation behavior in a Nb-5W-2Mo-1Zr niobium alloy fabricated by electron beam selective melting. Materials Characterization, 2021, 174: 111019. https://doi.org/10.1016/j.matchar.2021.111019.
[17] Zhang X, Fu T, Cui K, et al. The protection, challenge, and prospect of anti-oxidation coating on the surface of niobium alloy. Coatings, 2021, 11(7): 742. https://doi.org/10.3390/coatings11070742.
[18] Sun J, Li T, Zhang G P, et al. Different oxidation protection mechanisms of HAPC silicide coating on niobium alloy over a large temperature range. Journal of Alloys and Compounds, 2019, 790: 1014–1022. https://doi.org/10.1016/j.jallcom.2019.03.229.
[19] Hossain M D, Borman T, Oses C, et al. Entropy landscaping of high entropy carbides. Advanced Materials, 2021, 33(42): 2102904. https://doi.org/10.1002/adma.202102904.
[20] Tang X, Chong X, Feng J, et al. The role of entropy and enthalpy in high entropy carbides. Computational Materials Science, 2022, 210: 111474. https://doi.org/10.1016/j.commatsci.2022.111474.
[21] Shatynski S R. The thermochemistry of transition metal carbides. Oxidation of Metals, 1979, 13(2): 105–118. https://doi.org/10.1007/BF00611975.
[22] Gupta D K, Seigle L L. Free energies of formation of WC and W_2C, and the thermodynamic properties of carbon in solid tungsten. Metallurgical Transactions: A, 1975, 6(10): 1939–1944. https://doi.org/10.1007/BF02646859.
[23] Yang P J, Li Q J, Han W Z, et al. Designing solid solution hardening to retain uniform ductility while quadrupling yield strength. Acta Materialia, 2019, 179: 107–118. https://doi.org/10.1016/j.actamat.2019.08.024.
[24] Vishwanadh B, Krishna K V M, Upadhyay A, et al. Formation mechanism of the Nb_2C phase in the Nb-1Zr-0.1C (wt.%) alloy and interrelation between γ, β and α-Nb_2C carbide phases. Acta Materialia, 2016, 108: 186–196. https://doi.org/10.1016/j.actamat.2016.02.036.
[25] Vishwanadh B, Arya A, Tewari R, et al. Formation mechanism of stable NbC carbide phase in Nb-1Zr-0.1C (wt.%) alloy. Acta Materialia, 2018, 144: 470–483. https://doi.org/10.1016/j.actamat.2017.11.007.